The ARMM System - Autonomous Steering of Magnetically-Actuated Catheters: Towards Endovascular Applications

Christoff M. Heunis ⓘ, Yannik P. Wotte, Jakub Sikorski ⓘ, Guilherme Phillips Furtado ⓘ, and Sarthak Misra ⓘ

Abstract—Positioning conventional endovascular catheters is not without risk, and there is a multitude of complications that are associated with their use in manual surgical interventions. By utilizing surgical manipulators, the efficacy of remote-controlled catheters can be investigated *in vivo*. However, technical challenges, such as the duration of catheterizations, accurate positioning at target sites, and consistent imaging of these catheters using non-hazardous modalities, still exist. In this paper, we propose the integration of multiple sub-systems in order to extend the clinical feasibility of an autonomous surgical system designed to address these challenges. The system handles the full synchronization of co-operating manipulators that both actuate a clinical tool. The experiments within this study are conducted within a clinically-relevant workspace and inside a gelatinous phantom that represents a life-size human torso. A catheter is positioned using magnetic actuation and proportional-integral (PI) control in conjunction with real-time ultrasound images. Our results indicate an average error between the tracked catheter tip and target positions of 2.09 ± 0.49 mm. The median procedure time to reach targets is 32.6 s. We expect that our system will provide a step towards collaborative manipulators employing mobile electromagnets, and possibly improve autonomous catheterization procedures within endovascular surgeries.

Index Terms—Medical robots and systems, surgical robotics: steerable catheters/needles, surgical robotics: planning.
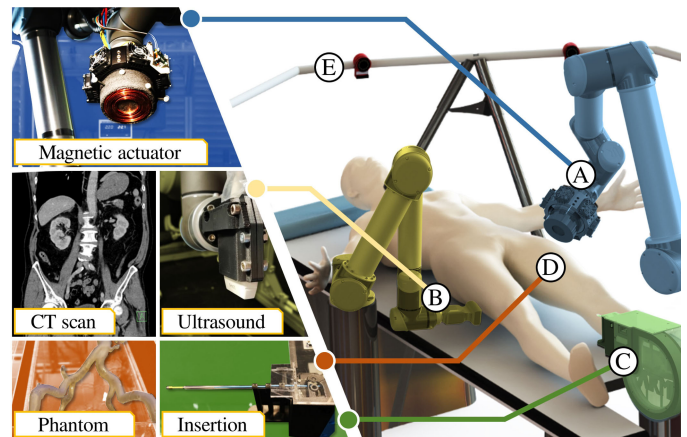

Fig. 1. The Advanced Robotics for Magnetic Manipulation (ARMM) system in a clinical setting. The system is envisioned to employ magnetic actuation to assist clinicians during endovascular interventions. Two manipulators respectively actuate an electromagnetic coil Ⓐ, and an ultrasound transducer Ⓑ. An automated catheter insertion device Ⓒ, inserts catheters into an arterial phantom model Ⓓ, fabricated from computed tomography (CT) images. The poses of all objects are tracked in real-time using a motion capture system Ⓔ.

I. INTRODUCTION

STEERING and positioning a catheter in target vessels during endovascular surgery is a challenging task [1]. In particular cases, standard interventions for endovascular repair involve high-risk complications, which can lead to unnecessary trauma during insertion [2]. Moreover, the accuracy of steering is highly dependent on the abilities of a clinician. A typical endovascular

intervention would involve the insertion of a catheter in the groin to access the heart or important arterial branches [3]. The catheter is, in most cases, tracked by utilizing X-ray imaging facilitated by the injection of contrast material, which discriminates the catheter from the arterial tree [4]. Despite its convenience, X-ray imaging causes additional safety risks due to the prolonged exposure of both patients and clinicians to ionizing radiation.

This brings to light two main complications in the clinical room, which are the limited diversity of actuation methods of surgical instruments, and the real-time visualization of such instruments in a hazard-free environment. Actuating surgical instruments by robotic and computer-aided means have experienced two major evolutions in the past decade. First, novel actuation methods, including the use of magnets for surgical instrument actuation, have advanced the endovascular industry in critical ways [5]–[8]. Next, when compared to human-in-the-loop actuation of surgical instruments, multiple serial-link robotic actuators (manipulators) have shown to offer decreased labor costs, a greater range of motion of instruments, and improved ergonomics for the clinician [9]–[12]. To support this notion, we have developed a novel and highly versatile system for the magnetic actuation of surgical instruments (Fig. 1).

The Advanced Robotics for Magnetic Manipulation (ARMM) system employs, amongst others a single, cored electromagnetic coil attached to a 6 degree-of-freedom (DoF) manipulator arm, which can be used to generate codirectional, prescribed magnetic fields and forces with independently controlled magnitudes [13]. Similar studies have been conducted on the remote steering of magnetic catheters. Charreyron *et al.* demonstrated a proof-of-concept for delivering drugs to precise locations inside the retina using a magnetic microcatheter [14]. The positioning accuracy of their system was limited by the workspace illumination conditions. Jeong *et al.* proposed a magnetically steerable guidewire using Helmholtz coils [15]. The guidewire was steered inside a phantom with five different arterial branches. Finally, a similar mobile electromagnetic coil system has been introduced that enables motion control of a magnetic catheter inside three-dimensional (3D) printed channels [16].

While the aforementioned studies have indicated a considerable amount of success in steering magnetic catheters, these tests were either executed within non-anthropomorphic mock-ups [16], or using computationally expensive mechanical models for catheters [15]. Furthermore, while accurate positioning of catheters has been reported to be between 1.9 ± 0.40 mm and 4.18 ± 1.76 mm under electromagnetic guidance, these studies have presented simplified scenarios in highly-controlled environments and small ($< 20 \times 30 \times 50$ cm^3) workspaces that deviate from clinically-relevant sizes [5], [17]. Finally, similar actuation systems have been designed to steer catheters at system bandwidths of 10–20 Hz [8]. This especially influences the duration of catheterization procedures, as indicated by Manstad *et al.*, who reported median durations of between 34.5–41.5 s for steering catheters to *in vivo* target sites [18]. To the best of our knowledge, no report has been found so far that demonstrates the integration of multiple surgical systems that operate autonomously at a higher bandwidth to achieve similar accuracies or durations. In this paper, we demonstrate that magnetic catheters can be autonomously actuated in a clinically-relevant environment. We achieve this within a larger workspace than that of the aforementioned studies, in a volume of 9 m^3. This environment includes a phantom with pulsating fluid flow, feedback from US images of the catheter tip, and two collaborative manipulators. We implement a simple, yet time-efficient approach that does not require an explicit model of the catheter mechanics. The catheter tip is controlled at a stable 30 Hz to reach targets provided by an end-user, and a US-based template matching algorithm.

This paper is organized as follows: Section II describes the serial-link manipulators and apparatus used in the ARMM system. Our gelatin phantom model, catheter insertion device, and magnetic endovascular catheter design are explained. This is followed by the control algorithms for magnetic actuation, as well as an outline of the path- and trajectory planning of the catheter tip and manipulators in Section III. In Section IV, we demonstrate the closed-loop control of the catheter in a clinically-relevant environment, followed by the results and a discussion of these results. Section V concludes this paper and provides directions for future work.

II. ADVANCED ROBOTICS FOR MAGNETIC MANIPULATION

This section describes the apparatus used in the ARMM system. The implemented methods result from two phases: pre-operative planning of a patient-specific arterial model, and intra-operative surgery involving catheterization.

A. The ARMM Manipulators

The ARMM system consists of two serial-link manipulators (Models UR5 and UR10, Universal Robots, Odense, Denmark). These manipulators employ a native interface of both manipulators to communicate with their own embedded controllers. These controllers execute the movement of the manipulators upon receiving a pose command, expressed as a set of joint velocities. A linear US L14-5 transducer (SonixTouch Q+, BK Medical, Quickborn, Germany) is mounted to the UR5 (hereinafter referred to as 'RobUltra'). The UR10 (referred to as 'RobARMM') carries an electromagnet capable of generating prescribed magnetic fields and gradients at the point of interest. The effective workspace of the ARMM system can be approximated by a sphere with a radius of 783 mm, though positioning the coil at a safe distance of 50 mm using RobARMM could allow for a maximum spherical workspace radius of 1300 mm. As the coil should be positioned outside the human body, we assume that the catheter is located between 50 mm and 200 mm away from the coil at any instance during the intervention. The coil can generate fields of at least 20 mT and gradients of more than 0.6 mT/mm, similar to the ones used in previous studies on magnetic catheters as discussed in our previous work [13].

B. Magnetic Actuation of Flexible Catheters

Magnetic interaction occurs between two principal agents: the dipole ($\mathbf{m} \in \mathbb{R}^3$) attached to the actuated device and the field ($\mathbf{B}(\mathbf{p}) \in \mathbb{R}^3$) at a point ($\mathbf{p} \in \mathbb{R}^3$) [19]. The magnetic catheter implemented within the ARMM system is actuated by varying the current supplied to the external electromagnetic coil. The current supply to the coil is controlled and amplified using a XenusPlus EtherCAT (XEL-230-40, Copley Controls, Canton, USA) amplifier. The actuated instrument is a commercial coronary guide catheter (Sherpa NX Active, Medtronic, Minneapolis, United States, diameter: 2 mm, length: 500 mm). The catheter shaft consists of low-density polyethylene (HDPE) with a stiffness of ± 1.5 N·m/rad and a hydrophilic surface coating to provide a smooth, low-friction surface. Five cylindrical magnets (NdFeB, diameter: 2 mm, length: 2 mm) are embedded in its tip.

A catheter insertion device (CID) is designed to continuously feed or retract catheters with sizes ranging from 3–34 Fr into the port of entry, such as an incision in the groin. The shaft of the catheter is gripped between a gear and bearing structure, and fed through a tube by a servo motor (MX-64AR Dynamixel, Robotis, South Korea). The insertion is done linearly with speeds ranging between 1.3–6.4 mm/s.

C. Arterial Phantom Model Fabrication

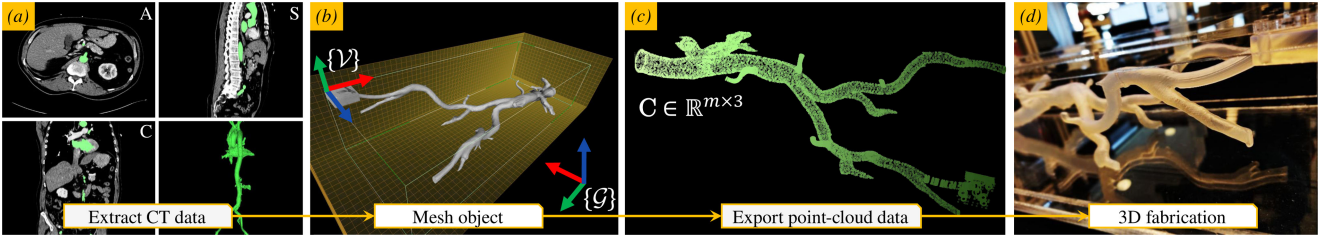An anthropomorphic phantom model of the human abdominal arteries is fabricated from raw pre-operative computed

Fig. 2. The fabrication process of the arterial phantom model. *(a)* Axial (A), sagittal (S) and coronal (C) views of a segmented scan of a male torso are extracted directly from computed tomography (CT) slices. Everything other than the vasculature of interest (green) has been masked. *(b)* The scan is then prepared as a mesh object in Meshlab (Visual Computing Lab, Pisa, Italy), and registered within the phantom reference frame ($\{\mathcal{V}\}$), before transformed to the global reference frame ($\{\mathcal{G}\}$). *(c)* The point-cloud dataset ($\mathbf{C} \in \mathbb{R}^{m \times 3}$), where m is the number of datapoints (40,212). *(d)* The final stereolithography (SLA) 3D-printed model, before being submerged in gelatin.

tomography (CT) data (Fig. 2(*a-d*)). CT slices of a 62-year old anonymous male torso (Medisch Spectrum Twente, Enschede, The Netherlands) are converted to a mesh object (Meshlab, Visual Computing Lab, Pisa, Italy), and imported to computer-aided design (CAD) software (Solidworks, Dassault Systemes, Tennessee) for editing. For our experiments, the external, internal and common iliac arteries through to the descending aorta are 3D-printed using stereolithography (SLA) and submerged in a mix of chemical gelatin and diluted water (80 g/L). Pulsating fluid flow is simulated through the arteries using a peristaltic pump (ISM 404, Ismatec, Wertheim, Germany). This fluid consists of a mixture of water, water-soluble silicone oil, and glycerin, which has been proven to approximate an appropriate sonographic appearance of blood flow in US images [20].

The reconstruction accuracy of the fabricated model is estimated by registering four known landmarks to a point-cloud dataset ($\mathbf{C} \in \mathbb{R}^{m \times 3}$) of the virtual arteries. These landmarks are registered in the ARMM workspace using an Optitrack Flex13 motion capture system (NaturalPoint Inc., Corvallis, USA). Next, the closest-point distances between the mesh vertices and points are measured in a mesh editing software (CloudCompare V211, EDF R&D, Corsica, France), resulting in a mean distance of 0.75 ± 0.08 mm. Finally, the transformation matrix between the point-cloud and the fabricated model is determined through an iterated closest point (ICP) algorithm [21]. US image acquisition is implemented during both the pre-operative and intra-operative phases to assist with US transducer calibration, 3D reconstruction, and catheter tip tracking. Cross-section brightness scans (B-scans) are acquired at a rate of 30 Hz, while 2D images (size 45×90 mm) are captured at a 10 MHz central frequency with a focus depth of $20-40$ mm and a maximum depth of 90 mm. The US transducer is rigidly connected to the RobUltra end-effector, which enables us to know its exact relative pose within the phantom reference frame ($\{\mathcal{V}\}$), and global coordinate frame ($\{\mathcal{G}\}$) (Fig. 2(*b*)). Reconstructing the phantom volume is done after extracting 2D images that geometrically correspond to the printed model on a precalculated trajectory. A 3-axis force sensor (K3D40, Mesysteme AG, Henningsdorf, Germany) is connected between the US transducer holder and the RobUltra end-effector. This allows us to control the desired contact force between the transducer surface and the phantom [22]. A series of volume pixels from binary US images are used as coordinates on a new point-cloud dataset [23]. The pose of RobUltra allows us to determine the

3D offset with respect to the phantom reference frame. We employ the aforementioned ICP method for determining the reconstruction accuracy of the US images, resulting in an overall mean error of 0.85 ± 0.56 mm. Finally, a 3D volume of the phantom is displayed on an interactive screen that allows the operator to select any target region, or 3D points of interest, within the phantom, with sub-millimeter precision.

III. CONTROL OF THE ARMM SYSTEM

In this section, we present the workflow as it occurs chronologically through the operative phases. We start by explaining the pre-operative US acquisition phase, followed by the path-planning of the catheter tip and the manipulators. Finally, the control strategy for the manipulators during the intra-operative phase is explained.

A. Ultrasound Reconstruction Using Hybrid Control

When the transducer travels along a trajectory on the phantom, we implement hybrid force-position control with a force of 2 N, in order to produce clear US images [24]. In the case that the transducer follows a trajectory in space, position control is used. Let us consider the tool pose of RobUltra, expressed as a position ($\mathbf{p}_u \in \mathbb{R}^3$) and angle-axis orientation ($\boldsymbol{\theta}_u \in \mathbb{S}^3$). The trajectory of the tool of the RobUltra end-effector is provided by a set of via-points ($i : 1 \to n$). We implement a modulated proportional-integral (PI) position-force and modulated proportional (P) orientation controller to realize a trajectory for this point, moved along the gelatine surface. Each point is reached with end-effector velocity ($\mathbf{V}_e$) provided by

$$\mathbf{V}_e = \mathbf{V}_d \left(1 - e^{-|\mathbf{E}|/R} \right) \hat{\mathbf{E}} + e^{-|\mathbf{E}|/R^5} \left(I \int_0^\infty \mathbf{E} \, \mathrm{d}t \right), \quad (1)$$

where $\mathbf{V}_d$ is the maximum tool velocity, $\mathbf{E} \in \mathbb{R}^3$ is the position error between $\mathbf{p}_{u,i}$ and $\mathbf{p}_{u,i+1}$, and R is a threshold for the stopping region. The term $(1 - e^{-|\mathbf{E}|/R})$ ensures continuity to avoid possible control artifacts caused by measurement noise. The end-effector orientation is described by two unit vectors ($\hat{\mathbf{q}}_{6,z} \in \mathbb{R}^3$ and $\hat{\mathbf{q}}_{6,y} \in \mathbb{R}^3$) which denote the z and y-axes of joint 6 of RobUltra. The desired angular velocity ($\boldsymbol{\omega}_e \in \mathbb{R}^3$) to minimize angular errors (θ_z and θ_y) in order to reach the final target orientation is given as follows:

$$\boldsymbol{\omega}_e = \omega_z \left(1 - e^{-|\theta_z|/\gamma} \right) \hat{\boldsymbol{\omega}}_z + \omega_y \left(1 - e^{-|\theta_y|/\gamma} \right) \hat{\boldsymbol{\omega}}_y, \quad (2)$$
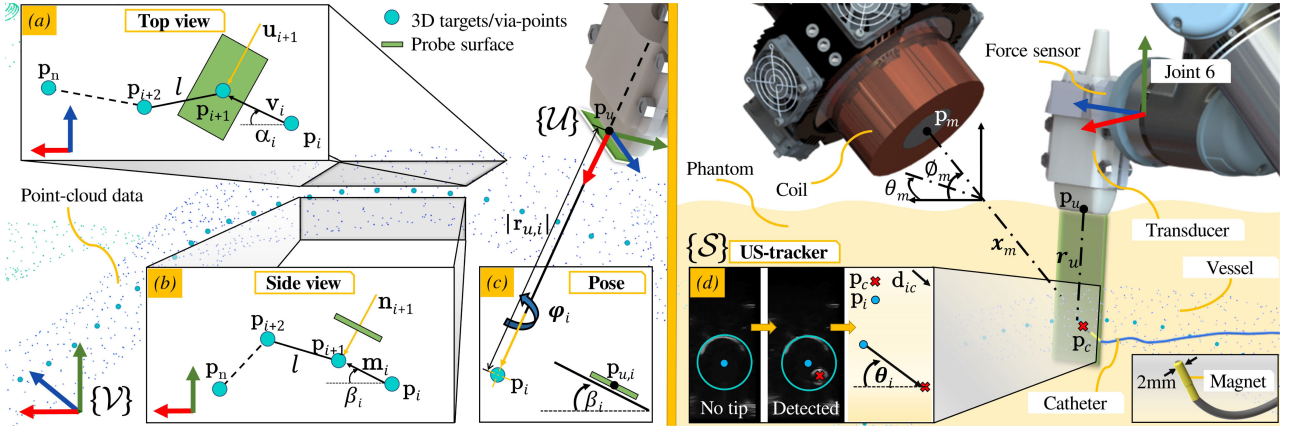
Fig. 3. A path consists of a set of 3D via-points ($\mathbf{p_n}$) for the catheter tip position ($\mathbf{p}_c$). We calculate the desired positions of the coil center point ($\mathbf{p}_m$) and of the ultrasound (US) transducer point ($\mathbf{p}_u$), as well as their respective distance vectors ($\mathbf{x}_m$) and ($\mathbf{r}_u$) to the catheter tip. *(a)* The xz-plane of the via-points showing target points ($\mathbf{p}_i$) for n targets. This allows for calculating the direction vector ($\mathbf{v}_i$) of a via-point ($i+1$), and its normal vector ($\mathbf{u}_{i+1}$) to derive the angle (α_i). *(b)* Similarly, the direction vector ($\mathbf{m}_i$), and its normal vector ($\mathbf{n}_{i+1}$) to the closest surface point are calculated to derive the inclination angle (β_i). *(c)* The angle (α_i) is used to calculate the rotation angle (φ_i) of the transducer at a target point ($\mathbf{p}_i$). The offset vector ($\mathbf{r}_{u,i}$) is calculated by the minimum Euclidean distance between these points. *(d)* The 2D catheter tip position is detected using a template-based detection algorithm. RobARMM (Universal Robots, Odense, Denmark) is positioned using spherical coordinates, where we define θ_m to be the azimuthal angle in the xz-plane from the x-axis and ϕ_m is the polar angle, from the positive y-axis. 2D US images are used to magnetically deflect the tracked tip (denoted by c) to the target via-point (denoted by i) by minimizing the error of the distance ($\mathbf{d}_{ic}$) between these two points.

where ω_z and ω_y are the maximum angular velocities of $\hat{\mathbf{q}}_{6,z}$ and $\hat{\mathbf{q}}_{6,y}$. The constant (γ) is analogous to R in (1). Provided the current ($\boldsymbol{\theta}_u^c$) and desired ($\boldsymbol{\theta}_u^i$) end-effector orientation, the desired angle (θ_z) and angular velocity ($\hat{\boldsymbol{\omega}}_z$) are given by

$$\theta_z = \arcsin\left(|\hat{\mathbf{q}}_{6,z}^c \times \hat{\mathbf{q}}_{6,z}^i|\right), \tag{3}$$

$$\hat{\boldsymbol{\omega}}_z = \frac{\hat{\mathbf{q}}_{6,z}^c \times \hat{\mathbf{q}}_{6,z}^i}{\sin(\theta_z)}. \tag{4}$$

Calculating θ_y requires a rotation matrix for a rotation by an angle (θ) about the unit vector ($\hat{\mathbf{k}}$), which yields

$$\theta_y = \arcsin |(\mathbf{R}_k(\theta_z, \hat{\boldsymbol{\omega}}_z)\hat{\mathbf{q}}_{6,y}^c) \times \hat{\mathbf{q}}_{6,y}^i|, \tag{5}$$

$$\hat{\boldsymbol{\omega}}_y = \mathbf{R}_k^{\mathrm{T}}(\theta_z, \hat{\boldsymbol{\omega}}_z)\frac{(\mathbf{R}_k(\theta_z, \hat{\boldsymbol{\omega}}_z)\hat{\mathbf{q}}_{6,y}^c) \times \hat{\mathbf{q}}_{6,y}^i}{\sin(\theta_y)}. \tag{6}$$

Finally, PI-force control between the transducer and phantom surface is implemented. Direct contact is ensured using a setpoint velocity ($\mathbf{V}(t)$) defined by

$$\mathbf{V}[k] = K_p\mathbf{f}_e[k] + K_i\mathbf{V}[k-1], \tag{7}$$

where the proportional gain (K_p) and the integral gain (K_i) are empirically determined to be 0.5 and 0.7 respectively, k describes the discrete time index, and $\mathbf{f}_e = (\mathbf{f}_d - \mathbf{f}_t)$ is the force error between the desired (d) and actual (t) tool forces, measured by the force sensor. For hybrid force-position control, we select the velocity component of the end-effector perpendicular to the gelatin surface (i.e. aligned with the x-axis of the transducer (Fig. 3), frame $\{\mathcal{U}\}$) to be controlled by force-control. The position error ($\mathbf{E}$) of (2) becomes

$$\mathbf{E}_{||} = \mathbf{E} - \hat{\mathbf{x}} \cdot (\hat{\mathbf{x}} \cdot \mathbf{E}), \tag{8}$$

where $\mathbf{E}_{||}$ is the position error component parallel to the surface and $\hat{\mathbf{x}}$ is the unit vector perpendicular to the surface. Finally, we traverse the generated trajectories with specified joint velocities—that is, we provide the resultant end-effector

velocity as an input to the manipulator. Using the task velocity in (1), joint velocities ($\dot{\mathbf{q}}$) are computed from the manipulator Jacobian ($\mathbf{J} \in \mathbb{R}^{6\times6}$) inverse approach, satisfying

$$\dot{\mathbf{q}} = \mathbf{J}^\dagger \mathbf{V}_e(\mathbf{p}_u). \tag{9}$$

$\mathbf{J}^\dagger$ denotes the damped pseudo-inverse of $\mathbf{J}$, given by [25]:

$$\mathbf{J}^\dagger = \mathbf{J}^{\mathrm{T}}(\mathbf{J}\mathbf{J}^{\mathrm{T}} + \rho^2\mathbf{I})^{-1}, \tag{10}$$

where ρ is the damping coefficient and $\mathbf{I} \in \mathbb{R}^{6\times6}$ is the identity matrix. Furthermore, we optimize the control parameters before executing experiments by simulating a dynamic model of RobUltra inside a virtual robot experimentation platform (V-REP) API framework (BlueZero, Blue Workforce, Aalborg, Denmark).

B. Intra-Operative Control

During the intra-operative phase, an end-user is required to select the final target point for the catheter tip within the phantom, the point-cloud of the anatomical part, as well as the distance ($l_{\max}$) between the via-points (Algorithm 1). As such, paths for the catheter tip are generated *a priori* to allow the catheter to reach its final target position ($\mathbf{p}_d \in \mathbb{R}^3$) inside the vessel volume. For our experiments, we implement a path planner that returns a matrix composed of 3D target points ($\mathbf{p}_n \in \mathbb{R}^{n\times3}$). This is done for n target points, each at the centroid of the surrounding artery. The resulting targets can be used as either a final target for the catheter tip or via-points ($\mathbf{p}_i \in \mathbb{R}^3$) between the insertion point and end-point, to generate trajectories for the manipulators.

Following this, we geometrically determine, for each via-point, the US transducer pose, described as an axis-angle rotation vector. We aim to position the transducer such that its center point coincides with the shortest distance vector between the desired via-point of the catheter tip, and the point of contact on the surface. Furthermore, it should be rotated to provide a
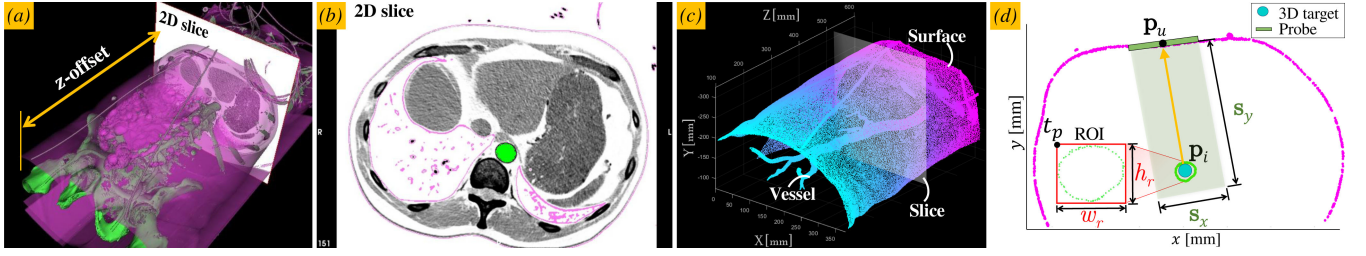
Fig. 4. Deriving the ultrasound (US) transducer pose from the point-cloud set: *(a)* Once a 3D target for the catheter tip is known, a 3 mm thick computed tomography (CT) slice is extracted at the z-offset. *(b)* The 2D view of the extracted slice, with the artery masked in green, and the surrounding soft tissue in pink. *(c)* The anatomical parts of interest are converted to an interactive 3D point-cloud set *(d)* The corresponding 2D point-cloud representation is a result from combining xyz-datapoints at each target in a 2D CT slice. This slice is used to determine the transducer center point ($\mathbf{p}_u$) by calculating the minimum distance (yellow arrow) from the surrounding points (pink) to the catheter tip target position ($\mathbf{p}_i$). The maximum US image width (S_x) and depth (S_y) is approximated by a planar workspace of 90×45 mm. Furthermore, the region of interest (ROI) is denoted by a bounding box with upper-left corner xy-position (t_p), width (w_r) and height (h_r).

Algorithm 1: 3D Path Planning for Catheter Tip (Prior to Insertion).

Inputs:
$\mathbf{C} \in \mathbb{R}^{m \times 3}$ ⇨ $[x,y,z]$ point-cloud matrix of the vessel in $\{\mathcal{V}\}$
$\mathbf{p}_d \in \mathbb{R}^3$ ⇨ Final 3D target point in the vessel
$l_{\max} \in \mathbb{R}^+$ ⇨ Constant distance between via-points

Output:
$\mathbf{p}_n \in \mathbb{R}^{n \times 3}$ ⇨ Path composed of $n \times 3$ via-points

Initialization:

1   *take mean of 2D coordinates in matrices* $\mathbf{C}[1:m;1,2]$ *and* $\mathbf{C}[1:m;1,3]$
$i := 1, k := 1$

   while $\mathbf{C}[i;1] < \mathbf{p}_d[1;1]$ **do** ⇨ Move window with size (r) through each element (i)

2    $\mathbf{s}_{xy} \leftarrow \frac{1}{r}\sum_{j=1}^{r}\mathbf{C}[1:j;1,2]$ ⇨ 2D vector for mean xy-coordinates

3    $\mathbf{s}_{xz} \leftarrow \frac{1}{r}\sum_{j=1}^{r}\mathbf{C}[1:j;1,3]$ ⇨ 2D vector for mean xz-coordinates

4    $\mathbf{p}_i \leftarrow [\mathbf{s}_{xz[i;1]}, \mathbf{s}_{xy[i;2]}, \mathbf{s}_{xz[i;2]}]$ ⇨ 3D point at each element
$i := i + 1$

   end

5   *concatenate all points* $\mathbf{p}_i$ *to form path* $\mathbf{p}_{old}$
remove points between via-points along distance l_{max}
$\mathbf{p}_k := \mathbf{p}_{old}[k,:], l := 0$ ⇨ Start with first 3D point
while $|norm(\mathbf{p}_d \_ \mathbf{p}_k)| > l_{max}$ **do**

   while $l < l_{max}$ **do**   ⇨ Calculate Euclidean distance (l) between each pair of via-points

6    $\mathbf{p}_{k+1} \leftarrow \mathbf{p}_{old}[k+1,:]$

7    $l \leftarrow |norm(\mathbf{p}_{k+1} - \mathbf{p}_k)|$
$k := k + 1$

   end

8    $\mathbf{p}_k \leftarrow \mathbf{p}_{old}[k,:]$

9    $\mathbf{p}_n \leftarrow \mathbf{p}_k$ ⇨ Update final path with 3D via-point

   $l := 0$

   end

---

true axial cross-section of the artery that is perpendicular to the vector between each via-point [26]. Thus, we again consider the point ($\mathbf{p}_u$), moving to a terminal point ($\mathbf{p}_{u,i}$) from the previous via-point ($\mathbf{p}_{u,i-1}$). Specifically, let $\mathbf{r}_{u,i} \in \mathbb{R}^3$ be the distance vector between the transducer point ($\mathbf{p}_{u,i}$) and the target point ($\mathbf{p}_i$). Using a closest-point detection algorithm on the 3D point-cloud dataset, we calculate the shortest distance between this target point, and the surrounding boundary xy-coordinates of the phantom surface. Then we derive the angle (Fig. 3(*a*))

$$\alpha_i = \frac{\mathbf{p}_{i+1,x} - \mathbf{p}_{i,x}}{\sqrt{(\mathbf{p}_{i+1,x} - \mathbf{p}_{i,x})^2 + (\mathbf{p}_{i+1,z} - \mathbf{p}_{i,z})^2}}, \quad (11)$$

to get the rotation angle (Fig. 3(*c*))

$$\varphi_i = \pi/2 - \alpha_i. \quad (12)$$

The transducer inclination angle (β_i) (Fig. 3(*b-c*)) is calculated similarly to (12). In our case, the phantom surface is assumed to be level, such that, for $\beta_i = 0$, the axis-angle rotation for the transducer ($\theta_{u,i}$) is calculated as

$$\theta_{u,i} = -\mathbf{v}_{u,i}\mathbf{R}_{\mathcal{V}}^{\mathcal{U}}\mathbf{R}(\beta_i, \varphi_i), \quad (13)$$

where $\mathbf{R}(\beta_i, \varphi_i) \in SO(3)$ is the input 3D rotation matrix and $\mathbf{R}_{\mathcal{V}}^{\mathcal{U}}$ is the rotation between the phantom and transducer frame. Furthermore, when the offset vector ($\mathbf{r}_{u,i}$) is known, we derive $\mathbf{v}_{u,i}$ using [27]:

$$\mathbf{v}_{u,i} = \mathbf{r}_{u,i}\cos(\varphi_i) + (\mathbf{k} \times \mathbf{r}_{u,i})\sin(\varphi_i)$$
$$+ \mathbf{k}(\mathbf{k} \cdot \mathbf{r}_{u,i})(1 - \cos(\varphi_i)), \quad (14)$$

where $\mathbf{k} \in \mathbb{R}^3$ represents the rotation vector (the x-axis of the transducer).

C. Ultrasound Image Template Matching Algorithm

Once the user defines a catheter target at a known offset on the phantom surface (Fig. 4(*a*)), the via-points for both the catheter and transducer are calculated. To establish proper insertion control, the catheter tip has to be tracked in the US images. Hence, we implement an OpenCV (version 3.4.8) image processing library to detect and track the catheter tip in each US frame of interest. The anatomical parts of interest can be masked and converted to a point-cloud dataset (Fig. 4(*b-c*)). Algorithm 2 and Fig. 4(*d*) describe a dynamic masking algorithm that provides, for each via-point, the region of interest (ROI) bounding box, based on the surrounding vessel geometry and the catheter target. The box parameters ($\mathbf{M}_n$) are used to crop the US slice, which provides the tracking algorithm with a smaller range of pixel coordinates. Once the first via-point has been reached by the transducer, the catheter insertion begins. The tracking process is illustrated in Fig. 5(*c*) and occurs as follows:

1) Match the cropped image with the user-defined template using the Pearson Correlation Coefficient method [28] (**I**);
2) Normalize the resulting proximity map (**II**);
3) Find the global minimum array elements and return their coordinates (**III**);
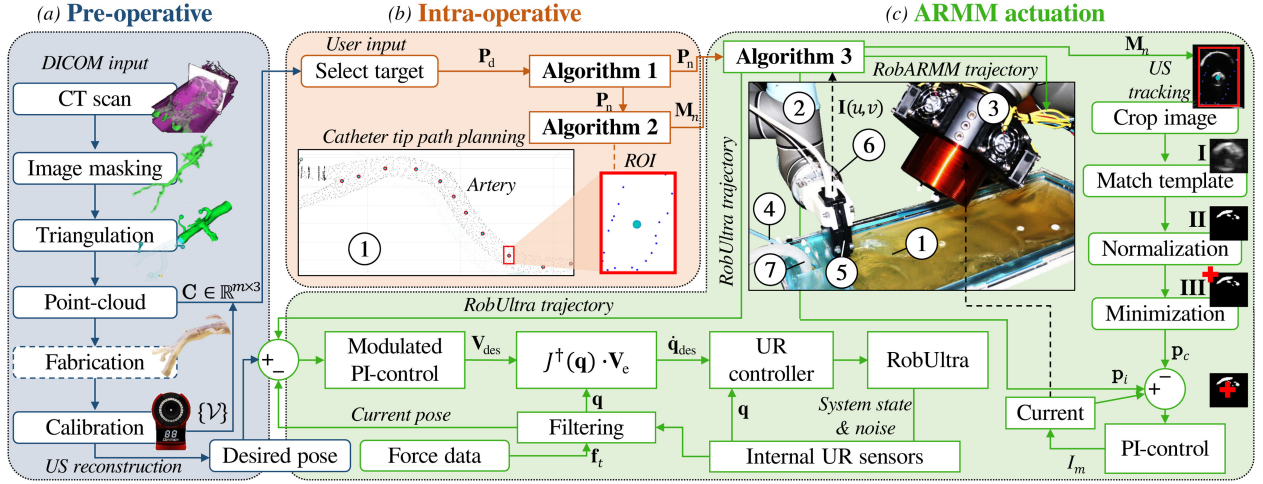
Fig. 5. Block diagram of the experimental setup: *(a)* During the pre-operative phase, an anatomical model is converted from a computed tomography (CT) scan to an interactive point-cloud dataset ($\mathbf{C} \in \mathbb{R}^{m \times 3}$). *(b)* During intra-operative planning, a user selects target locations, which are fed to the path planning algorithm (Algorithm 1), the region of interest (ROI) algorithm (Algorithm 2) and the actuation algorithm (Algorithm 3). *(c)* The setup shows the gelatine phantom model ①, with both manipulators (② UR5 (RobUltra) and ③ UR10 (RobARMM), Universal Robots, Odense, Denmark) in their initial configurations. The catheter is inserted using the catheter insertion device (CID) ④, while its tip can be either recognized or tracked on images obtained from the US transducer ⑤. The transducer is controlled using a force-position hybrid controller with the aid of a force sensor (K3D40, Mesysteme AG, Henningsdorf, Germany) ⑥. A peristaltic pump ⑦ simulates blood flow within the phantom. *Please refer to the accompanying video that describes the experimental setup and results.*

Algorithm 2: Region of Interest (ROI) Mask Generator.

Inputs:
$\mathbf{C} \in \mathbb{R}^{m \times 3}$ $\Rightarrow$ [*x,y,z*] point-cloud matrix of the vessel in $\{\mathcal{V}\}$
$\mathbf{p}_n \in \mathbb{R}^{n \times 3}$ $\Rightarrow$ Path composed of n via-points from the insertion point to the final target
$s_t \in \mathbb{N}$ $\Rightarrow$ Slice thickness of 3 mm

Output:
$\mathbf{M}_n \in \mathbb{R}^{n \times 4}$ $\Rightarrow$ Set of ROI bounding boxes, each with a 2D corner position (t_p), width (w_r), and height (h_r)

Initialization:
for $i := 1$ *to* n **do** $\Rightarrow$ Derive ROI for each point in path $\mathbf{p}_n$
1   *find all point indices (k) in point cloud within slice thickness* s_t
2    $k \leftarrow find(\mathbf{C}[1:m;1] > \mathbf{p}_i - \frac{s_t}{2}$ and $\mathbf{C}[1:m;1] < \mathbf{p}_i + \frac{s_t}{2})$
3    $t_p[i,:] \leftarrow [\min(\mathbf{C}[k_{min}:k_{max};3]), \max(\mathbf{C}[k_{min}:k_{max};2])]$
4    $w_r \leftarrow |\max(\mathbf{C}[k_{min}:k_{max};3]) - \min(\mathbf{C}[k_{min}:k_{max};3])|$
5    $h_r \leftarrow |\max(\mathbf{C}[k_{min}:k_{max};2]) - \min(\mathbf{C}[k_{min}:k_{max};2])|$
   $\mathbf{M}_i \leftarrow [t_p', w_r, h_r]$ $\Rightarrow$ parameters of ROI bounding box
end

Algorithm 3: Control Algorithm for Catheter Tip.

Inputs:
$\mathbf{p}_n \in \mathbb{R}^{n \times 3}$ $\Rightarrow$ Path composed of n via-points from the insertion point to final target
$\mathbf{C} \in \mathbb{R}^{m \times 3}$ $\Rightarrow$ [*x,y,z*] point-cloud matrix of the vessel in $\{\mathcal{V}\}$
$\mathbf{M}_n \in \mathbb{R}^{n \times 4}$ $\Rightarrow$ Set of region of interest bounding box with 2D corner position (t_p), width (w_r), and height (h_r)
$\mathbf{I}(u,v) \in \mathbb{N}$ $\Rightarrow$ Ultrasound image with rows (u) and columns (v)

Output:
$I_m \in \mathbb{Z}$ $\Rightarrow$ Current supply to the electromagnetic coil

Initialization:
$i := 1; k := 0; t_c := 0.01; dt := 0.08$
while $\mathbf{p}_i \neq \mathbf{p}_n$ **do**
1    $r_i \leftarrow \min(|norm(\mathbf{C}[i;2:3] - \mathbf{p}_i)|)$ $\Rightarrow$ Calculate minimum distance between via-point and top surface
2   *Derive UR5 pose using* (11)−(14) $\Rightarrow$ Position RobUltra on phantom
3   *Specify target length to CID* $\Rightarrow$ Insert catheter incrementally
   Crop $\mathbf{I}(u,v)$ *using* $\mathbf{M}_i$ $\Rightarrow$ Detect catheter tip within ROI and stop insertion
end
   $\mathbf{p}_i := \mathbf{p}_n$
4    $\mathbf{p}_c \leftarrow [t_p[i,1] + \frac{w_r}{2}, t_p[i,2] + \frac{h_r}{2}]$ $\Rightarrow$ Position RobARMM with respect to catheter tip
5    $\mathbf{d}_{ic} \leftarrow |norm(\mathbf{p}_c - \mathbf{p}_i)|)$ $\Rightarrow$ Calculate distance between tip and target
6    $\theta_i \leftarrow \mathrm{acos}\left(\frac{|\mathbf{p}_{i[2]} - \mathbf{p}_{c[2]}|}{d_{ic}}\right)$ $\Rightarrow$ Adjust RobARMM azimuthal angle in the xz-plane
   $\mathbf{d}_{f,k} := \mathbf{d}_{ic}; \mathbf{e}_{I,k} = 0$
while (*Experiment*) **do** $\Rightarrow$ While experiment is ON
7    $\mathbf{d}_{f,k} \leftarrow \frac{(\mathbf{d}_{ic,k} + \mathbf{d}_{f,k})^{t_c}/dt}{t_c/dt+1}$ $\Rightarrow$ Calculate filtered distance
8    $\mathbf{e}_{P,k} \leftarrow \mathbf{d}_{f,k}\left(\frac{(\mathbf{p}_{c[2]} - \mathbf{p}_{i[2]})}{\sqrt{(\mathbf{p}_{c[2]} - \mathbf{p}_{i[2]})^2 + 1e^{-6}}}\right)$ $\Rightarrow$ Calculate proportional error
9    $\mathbf{e}_{I,k} \leftarrow \mathbf{e}_{P,k}dt + \mathbf{e}_{I,k}$ $\Rightarrow$ Calculate integral error
10    $I_m \leftarrow K_P \mathbf{e}_{P,k} - K_I \mathbf{e}_{I,k}$ $\Rightarrow$ Prescribe input current
end

The returned pixel coordinates are then the matched template coordinates. In the case where the catheter merely has to be detected in order for autonomous insertion to continue, the template matching algorithm can be adapted to a detection algorithm by means of pixel intensity comparisons [29]. Each pixel coordinate ($s_p \in \mathbb{R}^2$) in the US slice is transformed to a corresponding location ($s_v \in \mathbb{R}^2$) in the coordinate frame $\{\mathcal{V}\}$. Finally, the catheter is deflected to the prescribed target using the ARMM magnetic actuation strategy.

D. ARMM Actuation Strategy for Flexible Catheters

In order to magnetically actuate an instrument, the ARMM system requires knowledge of the RobARMM end-effector pose, the magnetic field ($\mathbf{B}(\mathbf{p}) \in \mathbb{R}^3$) generated by the electromagnetic coil, as well as a point on the catheter tip ($\mathbf{p}_c \in \mathbb{R}^3$), at which the magnetic dipole ($\mathbf{m} \in \mathbb{R}^3$) attached to the instrument is located. Our actuation strategy (Algorithm 3) is to orient the coil so that $\mathbf{p} = \mathbf{p}_i$ is coincident with the coil symmetry axis ($\mathbf{Z}_C \in \mathbb{R}^3 : ||\mathbf{Z}_C|| = 1$) at all times [13]. We can express the magnetic field at $\mathbf{p}_i$ as

$$\mathbf{B}(\mathbf{p}_i, I_m) = \mathbf{Z}_C B(x_m, I_m), \qquad (15)$$

TABLE I
THE RESULTS OF THE 10 EXPERIMENTS, WHEREIN THE CATHETER IS INSERTED INTO THE ARTERIAL PHANTOM, AND DEFLECTED TO PRESCRIBED 3D TARGETS.
THE RED BOUNDING BOXES INDICATE THE RECONSTRUCTED REGIONS OF INTEREST (ROIs) FOR EACH TARGET. THE STARTING OFFSET BEFORE DEFLECTION IS
SHOWN. NEXT, THE INSERTION LENGTH OF THE CATHETER AT THE TARGET AND THE CUMULATIVE EXECUTION TIME TO REACH THE REGION ARE INDICATED.
THIS IS FOLLOWED BY THE ACCURACY (AVERAGE DISTANCE BETWEEN THE TARGET AND THE CATHETER TIP), AND THE STANDARD
DEVIATION (σ) OF THE ACCURACY.

Offset [mm]	4.32	3.81	3.16	4.38	5.51	5.70	5.61	6.57	8.08	11.17
Insertion [mm]	15.25	25.48	35.65	50.93	71.36	86.70	102.13	208.73	223.96	239.19
Execution [s]	10.02	13.78	21.20	29.94	50.68	59.80	64.87	97.16	101.03	111.80
Accuracy [mm] (σ [mm])	2.32 (0.25)	2.05 (0.27)	1.04 (0.31)	1.91 (0.32)	2.07 (0.95)	3.97 (0.41)	2.01 (0.65)	1.98 (0.34)	2.14 (0.97)	1.41 (0.39)

where $I_m \in \mathbb{R}$ is the current input to the electromagnetic coil, $x_m \in \mathbb{R}^+$ is the distance from the dipole (on the catheter tip position) to the face of the coil, and $B(x_m, I_m)$ is the scalar value of the magnetic field along the coil symmetry axis.

We aim to influence the bending of the catheter by applying the external magnetic wrench, such that its tip moves towards the desired location. With a prescribed offset distance, the coil pose with respect to the catheter tip frame is expressed in spherical coordinates ($\mathbf{s_m} = \begin{bmatrix} x_m & \theta_m & \phi_m \end{bmatrix}$), defined as shown in Fig. 3. We account for the distance ($\mathbf{d}_{ic}$) between the desired ($\mathbf{p}_i(z, y)$) and actual ($\mathbf{p}_c(z, y)$) catheter tip positions using a linear PI-controller on the electromagnetic coil current, with feedback provided by the US images.

To account for sudden position jumps, a filtered distance ($\mathbf{d}_{f,k}$) between two points is obtained by the application of a first-order filter (using the discrete-time index k) on the estimated distance ($\mathbf{d}_{ic}$) - see Algorithm 3, Line 7. The proportional error ($\mathbf{e}_{P,i}$) and integral error ($\mathbf{e}_{I,i}$) are calculated as shown in Algorithm 3, Line 8 and Line 9 respectively. We continuously update the demand current for the electromagnetic coil (Line 10), where K_P and K_I are proportional gains of the PI controller. Based on empirical tests, these gains are set to 0.12 A/mm and 0.05 A/mm^2.

IV. EXPERIMENTS

This section describes the experimental setup used to validate our proposed actuation strategy. Furthermore, it reports on the experimental results that were achieved to validate the overall positioning accuracy of the ARMM system.

A. Experimental Setup

The poses of the manipulators and other objects within the ARMM workspace are monitored in real-time using the motion tracking system. Any movement within the system is registered by the means of passive markers - retroreflective spheres that are triangulated by the surrounding cameras. We register all objects inside the ARMM workspace and derive the transformation of the coordinates from the tracking system reference frame to the global reference frame ($\{\mathcal{G}\}$). Furthermore, we specify three additional frames - that of the US transducer tip ($\{\mathcal{U}\}$), the US image plane ($\{\mathcal{S}\}$) and the arterial phantom ($\{\mathcal{V}\}$) (Fig. 3).

An experiment is conducted using the block diagram shown in Fig. 5. Within this experiment, a magnetic catheter is inserted into a phantom in order to reach a 3D target inside the arteries. Fluid flow within the artery is set to a speed of 17.6 cm/s. An end-user initializes the user interface associated with the particular CT-data data of the phantom and selects a target in 3D interactively on the point-cloud. This target is then sent to the ARMM controller, which calculates the desired end-effector poses and trajectories for both the manipulators. This strategy is repeated for 10 different targets.

B. Results

The results of all 10 trials are reported in Table I. During the experiment, the catheter successfully reached the prescribed targets. The average targeting error between the tracked tip and target positions is 2.09 ± 0.49 mm. These errors are slightly higher than previously reported *ex-vivo* results using similar magnetic actuation systems [5], [17]. However, the experiments presented therein either involved the deflection of a catheter in free air, or under the guidance of external cameras (which have a higher resolution than US, but nonetheless incompatible with clinical use). Next, a study with nearly identical equipment than ours reported *in vivo* accuracies of 4.18 ± 1.76 mm under electromagnetic guidance [18], which is less precise than the method presented in this paper. Thus, the US-guided actuation method in the ARMM system is more promising and, moreover, achieves a stable maximum bandwidth of 30 Hz, which is higher than that of similar actuation systems [8].

The process of acquiring a new US image and applying the target tracking algorithm introduces an average latency of about 273 ms. A slice is acquired within 50 ms and target tracking needs approximately 230 ms, which suggests that most of the latency is due to transferring the images to the user interface for real-time display. Secondly, the median procedure time to reach via-points, and to stabilize the catheter tip at the 3D targets is 32.6 s. This is comparable to [18], who reported median durations of 34.5 s using electromagnetic guidance, and 41.5 s using fluoroscopy images of an identic iliac vascular phantom. The manipulators are both able to reach their prescribed poses at each via-point during the insertion. Consequently, autonomous insertion was achieved from the insertion point to the final target

at a 100% success rate, while full control of the catheter tip was implemented at the final target. The hybrid force-position controller implemented on RobUltra resulted in a mean position error of the transducer of 1.48 ± 0.65 mm and can move at a maximum speed of 12 mm/s. We noticed that the accuracy in the positioning was directly coupled to robustness in the tracking algorithm, which is limited to the imaging depth (90 mm) of the L14-5 transducer.

V. CONCLUSIONS & FUTURE WORK

This study investigates the benefits of a model-free catheterization approach for a novel magnetic actuation system. In this approach, a magnetic endovascular catheter is guided towards and positioned at user-defined targets inside an arterial phantom, while relying on US images. The methods presented in this study could allow clinicians with limited experience to insert and position endovascular catheters within the human body at average positioning errors of 2.09 ± 0.49 mm.

In our future work, we plan to reduce positioning errors that may result from angular displacements within pulsating fluid flow. This can be accounted for either by employing adaptive control methods or by means of independent magnetic field and gradient control, as discussed in [13]. Next, we plan to demonstrate the ARMM actuation strategy in a tele-operative manner which, in practice, would further reduce the risks imposed by both intermittent X-ray scans during an intervention and prolonged catheterization durations. A real-time vessel tracking method of the target arteries, while compensating for breathing-induced motions should be incorporated. Finally, we will develop improved catheter detection and tracking algorithms by reducing acoustic clutter and improving the resolution of the US images. Consequently, it could aid with reconstructing arteries within non-homogeneous environments and allow for improved control over both insertion and positioning.

REFERENCES

[1] K Abdelaal *et al.*, "4Fr in 5Fr sheathless technique with standard catheters for transradial coronary interventions: Technical challenges and persisting issues," *Catheterization Cardiovascular Interv.*, vol. 85, no. 5, pp. 809–815, 2015.

[2] Health Quality Ontario, "Coil embolization for intracranial aneurysms: An evidence-based analysis," *Ontario Health Technol. Assessment Ser.*, vol. 6, no. 1, pp. 1–114, 2006.

[3] M. Ikhsan, K. K. Tan, and A. S. Putra, "Assistive technology for ultrasound-guided central venous catheter placement," *J. Med. Ultrason.*, vol. 45, no. 1, pp. 41–57, 2018.

[4] A. Hernandez-Vela *et al.*, "Accurate coronary centerline extraction, caliber estimation, and catheter detection in angiographies," *IEEE Trans. Inf. Technol. Biomedicine*, vol. 16, no. 6, pp. 1332–1340, Nov. 2012.

[5] J. Sikorski, A. Denasi, G. Bucchi, S. Scheggi, and S. Misra, "Vision-based 3D control of magnetically actuated catheter using BigMag - an array of mobile electromagnetic coils," *IEEE/ASME Trans. Mechatronics*, vol. 24, no. 2, pp. 505–516, Apr. 2019.

[6] B. Véron, A. Hubert, J. Abadie, and N. Andreff, "Geometric analysis of the singularities of a magnetic manipulation system with several mobile coils," in *Proc. IEEE/RSJ Int. Conf. Intell. Robots Syst.*, Tokyo, Japan, Nov. 2013, pp. 4996–5001.

[7] J. Rahmer, C. Stehning, and B. Gleich, "Remote magnetic actuation using a clinical scale system," *PloS ONE*, vol. 13, no. 3, pp. 1–19, 2018.

[8] C. Heunis, J. Sikorski, and S. Misra, "Flexible instruments for endovascular interventions: Improved magnetic steering, actuation, and image-guided surgical instruments," *IEEE Robot. Autom. Mag.*, vol. 25, no. 3, pp. 71–82, Sep. 2018.

[9] N. Preda, A. Manurung, O. Lambercy, R. Gassert, and M. Bonfè, "Motion planning for a multi-arm surgical robot using both sampling-based algorithms and motion primitives," in *Proc. IEEE/RSJ Int. Conf. Intell. Robots Syst.*, Hamburg, Germany, Sep. 2015, pp. 1422–1427.

[10] Abbou *et al.*, "Laparoscopic radical prostatectomy with a remote controlled robot," *J. Urology*, vol. 197, no. 2, pp. S210–S212, 2017.

[11] L. B. Kratchman, T. L. Bruns, J. J. Abbott, and R. J. Webster, "Guiding elastic rods with a robot-manipulated magnet for medical applications," *IEEE Trans. Robot.*, vol. 33, no. 1, pp. 227–233, Feb. 2017.

[12] P. R. Slawinski, A. Z. Taddese, K. B. Musto, K. L. Obstein, and P. Valdastri, "Autonomous retroflexion of a magnetic flexible endoscope," *IEEE Robot. Autom. Lett.*, vol. 2, no. 3, pp. 1352–1359, Jul. 2017.

[13] J. Sikorski, C. M. Heunis, F. Franco, and S. Misra, "The ARMM system: An optimized mobile electromagnetic coil for non-linear actuation of flexible surgical instruments," *IEEE Trans. Magn.*, vol. 55, no. 9, Sep. 2019, Art. no. 5600109.

[14] S. L. Charreyron, B. Zeydan, and B. J. Nelson, "Shared control of a magnetic microcatheter for vitreoretinal targeted drug delivery," in *Proc. IEEE Int. Conf. Robot. Autom.*, May, 2017, pp. 4843–4848.

[15] Jeong *et al.*, "Feasibility study on magnetically steerable guidewire device for percutaneous coronary intervention," *Int. J. Control, Autom. Syst.*, vol. 15, pp. 473–479, 2017.

[16] L. Yang, X. Du, E. Yu, D. Jin, and L. Zhang, "Deltamag: An electromagnetic manipulation system with parallel mobile coils," in *Proc. IEEE Int. Conf. Robot. Autom.*, Montreal, Canada, May, 2019, pp. 9814–9820.

[17] J. Edelmann, A. J. Petruska, and B. Nelson, "Magnetic control of continuum devices," *Int. J. Robot. Res.*, vol. 36, no. 1, pp. 68–85, 2017.

[18] F. Manstad-Hulaas, G. A. Tangen, L. G. Gruionu, P. Aadahl, and T. A. Hernes, "Three-dimensional endovascular navigation with electromagnetic tracking: *Ex vivo* and *in vivo* accuracy," *J. Endovascular Therapy*, vol. 18, no. 2, pp. 230–240, 2011.

[19] A. J. Petruska and J. J. Abbott, "Optimal permanent-magnet geometries for dipole field approximation," *IEEE Trans. Magn.*, vol. 49, no. 2, pp. 811–819, Feb. 2013.

[20] Yoshida *et al.*, "Blood-mimicking fluid for the doppler test objects of medical diagnostic instruments," in *Proc. IEEE Int. Ultrasonics Symp.*, Dresden, Germany, Oct. 2012, pp. 1–4.

[21] D. Holz, A. E. Ichim, F. Tombari, R. B. Rusu, and S. Behnke, "Registration with the point cloud library: A modular framework for aligning in 3-D," *IEEE Robot. Autom. Mag.*, vol. 22, no. 4, pp. 110–124, Dec. 2015.

[22] P. Chatelain, A. Krupa, and N. Navab, "Optimization of ultrasound image quality via visual servoing," in *Proc. IEEE Int. Conf. Robot. Autom.*, Seattle, USA, May 2015, pp. 5997–6002.

[23] V. Chougule, A. Mulay, and B. B Ahuja, "Conversions of CT scan images into 3D point cloud data for the development of 3D solid model using B-Rep scheme," in *Proc. Int. Conf. Precision, Meso, Micro Nano Eng.*, Calicut, India, Dec. 2013, pp. 630–635.

[24] K. Mathiassen, J. E. Fjellin, K. Glette, P. K. Hol, and O. J. Elle, "An ultrasound robotic system using the commercial robot UR5," *Frontiers Robot. AI*, vol. 3, pp. 1–16, 2016.

[25] S. Chiaverini, B. Siciliano, and O. Egeland, "Review of the damped least-squares inverse kinematics with experiments on an industrial robot manipulator," *IEEE Trans. Control Syst. Technol.*, vol. 2, no. 2, pp. 123–134, Jun. 1994.

[26] B. Ihnatsenka and A. P. Boezaart, "Ultrasound: Basic understanding and learning the language," *Int. J. Shoulder Surgery*, vol. 4, no. 3, pp. 55–62, 2010.

[27] R. M. Murray, *A Mathematical Introduction to Robotic Manipulation*. Boca Raton, FL, USA: CRC Press, 2017, pp. 27–29.

[28] Z. Pan and X. Wang, "Correlation tracking algorithm based on adaptive template update," in *Proc. 3rd Int. Congr. Image Signal Process.*, Yantai, China, Oct. 2010, pp. 98–101.

[29] N. Markus, Mi. Frljak, I. S. Pandzic, J. Ahlberg, and R. Forchheimer, "A method for object detection based on pixel intensity comparisons," in *Proc. 2nd Croatian Comput. Vision Workshop*, 2013, pp. 1–5.